Materials Characterization 191 (2022) 112130

Contents lists available at ScienceDirect

Materials Characterization

journal homepage: www.elsevier.com/locate/matchar

Surface finishing effects on the corrosion behavior and electrochemical activity of 2098-T351 aluminum alloy investigated using scanning microelectrochemical techniques

Rejane Maria P. da Silva [a,*], Mariana X. Milagre [a], Javier Izquierdo [b,c], Abenchara Maria Betancor-Abreu [b], Leandro A. de Oliveira [d], João Victor de S. Araujo [a], Renato A. Antunes [d], Ricardo M. Souto [b,c,**], Isolda Costa [a,*]

[a] Instituto de Pesquisas Energéticas e Nucleares - IPEN/CNEN, Av. Prof. Lineu Prestes, 2242 São Paulo, Brazil
[b] Department of Chemistry, Universidad de La Laguna, P.O. Box 456, E-38200 La Laguna (Tenerife), Canary Islands, Spain
[c] Institute of Materials Science and Nanotechnology, Universidad de La Laguna, P.O. Box 456, E-38200 La Laguna (Tenerife), Canary Islands, Spain
[d] Centro de Engenharia, Modelagem e Ciências Sociais Aplicadas (CECS), Universidade Federal do ABC (UFABC), Av. dos Estados 5001, 09210-580 Santo André, SP, Brazil

ARTICLE INFO

Keywords:
Al-cu-Li alloy
Surface preparation effects
Microelectrochemical techniques
Localized corrosion
NSDL
Electrochemical activity

ABSTRACT

The effects of surface finishing on the corrosion behavior and electrochemical activity of AA2098-T351 (Al–Cu–Li alloy) were investigated on the basis of the correlation between surface chemistry, microstructure and electrochemical activity. The alloy was evaluated in the as-received and polished conditions. The morphology of the two types of surfaces was investigated using confocal laser scanning microscopy (CLSM), optical microscopy and optical 3D profilometry. The surface chemistry was analyzed by X-ray photoelectron spectroscopy (XPS) and energy dispersive X-ray spectroscopy (EDX). Scanning microelectrochemical techniques (namely, localized electrochemical impedance spectroscopy (LEIS), the scanning vibrating electrode technique (SVET) and scanning electrochemical microscopy (SECM) in potentiometric mode) were used to examine the electrochemical activity of the surfaces. The results showed that on the as-received surface, the near surface deformed layer (NSDL), which is composed of Mg-rich bands, influenced the corrosion activity of the alloy. Higher electrochemical activity and greater susceptibility to severe localized corrosion were related to the polished surface condition compared to the as-received one.

1. Introduction

Al-Cu-Li alloys are advanced materials for aerospace applications due to their attractive mechanical properties and low density compared with conventional aluminum alloys. Lithium is added to provide weight reduction [1,2] and therefore fuel economy. These wrought alloys are rolled during plate manufacturing and this process induces a near-surface deformed layer (NSDL) on the surface of the alloy due to contact of the alloy with the rolling rolls. This NSDL has chemical and microstructural characteristics different from the bulk of the wrought alloy [3–7]. The characteristics of NSDL affect the corrosion behavior of Al alloys, as it is informed in the literature [5,6,8,9]. It presents a corrosion behavior different from that of the bulk alloy [3]. Although the effects of NSDL and mechanical grinding on the corrosion susceptibility of different aluminum alloys have been investigated [5,8,10–16], studies on the influence of NSDL on the corrosion behavior of Al–Cu–Li alloys, especially AA2098-T351, used in this study, are scarce.

The AA2098 alloy was developed to replace conventional 2XXX series aluminum alloys [17] to reduce aircraft weight and therefore fuel consumption. This alloy belongs to the 3rd generation of Al–—Li alloys and, according to the literature [18,19], it has good mechanical resistance, tenacity and low density. Its chemical composition, which contains Cu, Li, Mg, Ag, Zr, Si, and Fe, is responsible for the development of an advanced microstructure with precipitation of hardening phases, such as the T1 phase (Al_2CuLi) [20]. This phase has been reported as the main strengthening phase in Al-Cu-Li alloys. It precipitates

* Corresponding authors at: Instituto de Pesquisas Energéticas e Nucleares - IPEN/CNEN, Av. Prof. Lineu Prestes, 2242 São Paulo, Brazil.
** Correspondence to: Ricardo M. Souto, Department of Chemistry, Universidad de La Laguna, P.O. Box 456, E-38200 La Laguna, Tenerife, Canary Islands, Spain.
E-mail addresses: rejane.silva@ipen.br (R.M.P. da Silva), rsouto@ull.es (R.M. Souto), icosta@ipen.br (I. Costa).

https://doi.org/10.1016/j.matchar.2022.112130
Received 25 March 2022; Accepted 13 July 2022
Available online 16 July 2022

preferentially at grain/subgrain boundaries and inside grains. Its precipitation depends on the level of deformation before the aging process [21]. Although the T1 phase imparts good mechanical properties to Al-Cu-Li alloys, it can adversely affect the corrosion resistance of the alloy corrosion due to its Li content [22–24]. Several studies have shown that Al-Cu-Li alloys are very sensitive to localized corrosion [25–29]. According to Ma et al. [30,31], the corrosion mechanism of Al-Cu-Li alloys is associated with the T1 phase and the constituent micrometric particles. The corrosion induced by the constituent particles is generally superficial and varies with the Cu content of the particles. On the other hand, the preferential attack of the T1 phase is associated with severe localized corrosion (SLC) which is characterized by rings of corrosion products surrounding the pits and evolution of hydrogen gas from these sites.

In a previous work [32], the effect of NSDL induced by the manufacturing process on the corrosion behavior of aluminum alloy 2198-T851 was studied using conventional (i.e., surface averaging) electrochemical techniques. NSDL was found to be more active than the bulk alloy, but the attack associated with it was only superficial compared to the same alloy with a mechanically polished surface, in which severe localized corrosion (SLC) associated with the T1 phase was observed [32].

The application of local electrochemical techniques to study the influence of the near-surface deformed layer (NSDL) on the local electrochemical activities of Al-Cu-Li alloys is still scarce in the literature. Localized electrochemical techniques, such as scanning electrochemical microscopy (SECM), local electrochemical impedance spectroscopy (LEIS), and scanning vibrating electrode technique (SVET), have been successfully used to study the corrosion behavior of Al-Cu-Li alloys [23,33–35]. These scanning probe techniques present interesting electrochemical and spatial selectivities, and can provide complementary information. LEIS is a powerful tool to study local electrochemical activity [36,37], and it has been applied to study local electrochemical behavior of pure Cu–—Al and Al–—Mg systems, as well as more complex Al alloys, by combining experimental and/or simulation approaches [38–43]. SVET measures local ionic currents by means of a vibrating probe close to a reactive surface [44], which makes it possible to monitor the sensitivity of Al-Cu-Li alloys to localized corrosion [23,34]. On the other hand, electrochemical responses are monitored by SECM [45] using various operation modes, which can be broadly classified as amperometric or potentiometric, depending on the type of probe used (i.e., a microelectrode (UME) or an ion selective microelectrode (ISME), respectively) [46]. Although SECM in amperometric operation mode has already been used to characterize the electrochemical activity of Al-Cu-Li alloys [33,34,47], studies using the combination of amperometric and potentiometric SECM probes to characterize this type of material are rare to date [35,48]. A very interesting option has opened up with the development of solid contact Mg ion selective microelectrodes (ISME) suitable for potentiometric SECM imaging. In this way, images of Mg^{2+} distributions on corroding Mg surfaces were obtained by potentiometric measurements [49].

In this context, the present work aims to study the influence of surface finishing conditions on the corrosion susceptibility and electrochemical activity of AA2098-T351. For this purpose, samples of the Al-Cu-Li alloy were studied under the conditions as they were received (with NSDL) or polished (without NSDL) exposed to a NaCl solution. The corrosion behavior was studied by immersion tests and scanning microelectrochemical techniques (namely, SVET, LEIS, and SECM in potentiometric operation using a solid contact magnesium ion-selective microelectrode (Mg^{2+} ISME) to monitor Mg^{2+} distributions on AA2098-T351 in the as-received or the polished surface conditions. The use of various scanning microelectrochemical techniques to study the influence of the surface finish state on the local electrochemical activities of AA2098-T351 has not been reported in the literature. These contribute to the body of spatially resolved knowledge on the corrosion behavior and electrochemical activity of Al-Cu-Li alloys.

2. Experimental

2.1. Material

AA2098-T351 alloy (wt%: 3.4 Cu, 1.0 Li, 0.3 Mg, 0.3 Ag, 0.4 Zr, 0.04 Fe, 0.05 Si, 0.02 Zn, 0.003 Mn) was evaluated under as-received and polished conditions. For the polished samples, the surfaces were successively ground with 320, 550, 800, 1200 and 4000 grit SiC paper, then polished using diamond slurries of 3 μm and 1 μm.

2.2. Microstructural and surface characterization

Surface characterization was performed on polished and as-received samples. Confocal laser scanning microscopy (CLSM) analysis was performed using a LEXT OLS4100 microscope (Olympus, Shinjuku, Tokyo, Japan) and a DMLM optical microscope coupled to an EC3 camera and controlled by LASES software (Leica, Wetzlar, Germany). Energy Dispersive X-ray Spectroscopy (EDX) analyzes were performed using a JSM-6010LA microscope (JEOL, Akishima, Tokyo, Japan).

The chemical composition of the AA2098-T351 surfaces was evaluated by X-ray photoelectron spectroscopy (XPS), before and after the corrosion tests. A K-alpha+ spectrometer (Thermo Fisher Scientific, Waltham, MA, USA) was used which operated with a monochromatic Al-Kα X-ray source. The pressure in the analysis chamber was about 10^{-7} Pa. The binding energy scale was calibrated based on the adventitious C1s peak at 284.8 eV. The profilometry images and the corresponding penetration profiles were obtained using a ZESCOPE model optical profilometer (Zemetrics, Tucson, AZ, USA).

Monitoring of the corrosion process on the surfaces of AA2098-T351 was carried out by means of immersion tests in 5 mmol L^{-1} of NaCl solution at ambient temperature. The surfaces were examined for different periods of time up to 16 h of immersion.

2.3. Scanning electrochemical microscopy (SECM)

Potentiometric operation was available using high-resolution SECM equipment (Sensolytics, Bochum, Germany), coupled to an Autolab electrochemical interface (Metrohm, Herisau, Switzerland), controlled by a conventional computer. Additionally, a voltage follower based on a 10^{13} Ω input impedance operational amplifier (TL071, Texas Instruments, Dallas, TX, USA) was added in the measurement circuit. Potentiometric measurements were performed at room temperature using this setup. The AA2098-T351 surfaces were left in their spontaneous open circuit (i.e. they remained effectively unbiased during the measurements).

A magnesium ion-selective microelectrode (Mg^{2+} ISME), with solid-contact, was employed to monitor the Mg^{2+} distributions that develop on AA2098-T351 samples. The Mg^{2+} ISME was made from micropipettes by pulling borosilicate capillaries (outer Ø = 1.5 mm, wall thickness Ø = 0.225 mm, purchased from Hilgenberg GmbH, Malsfeld, Germany), using a model P-30 micropipette puller (Sutter Instrument, Novato, CA, USA). The borosilicate glass capillaries were pre-soaked in a "piranha solution" and thoroughly washed with deionized water and ethanol, then dried in an oven at 80 °C for 120 min. The inner wall of the micropipette tip was rendered hydrophobic using 5% dimethyldichlorosilane in heptane. This procedure was carried out by exposing the tip of the micropipette to the solution by capillary action and then kept in an oven at 80 °C for 90 min in a closed Petri dish.

The ionophore cocktail employed in the fabrication of the Mg^{2+} ISME consisted of poly(vinyl chloride) (PVC): potassium tetrakis (4-chlorophenyl) borate (PTCB): bis-N,N-dicyclohexyl-malonamide: 2-nitrophenyl octyl ether (NPOE) in the ratio 13:7:7.5:472 (w/w, mg). Tetrahydrofuran (THF) (1.0 mL) was used for component dissolution. The ionophore cocktail was inserted into the micropipette under suction. Then, the THF was allowed to evaporate for about 40 h at room temperature.

The internal contact with the cocktail was made using carbon fiber (approximately 30 μm in diameter), cut to 3.0 cm in length. A Cu wire (about 12 cm in length and 0.5 mm in diameter) was connected to the carbon fiber using silver epoxy to provide electrical contact. The carbon fiber to be inserted into the cocktail was then coated with a conductive PEDOT polymer. For this, an electrochemical cell composed of an Ag/AgCl wire as reference electrode, a Pt wire as the auxiliary electrode and the carbon fiber as working electrode was employed. The monomer 3,4-ethylenedioxythiophene dissolved in $BMIM^{+}$ PF_6^{-} ionic liquid was used as electrolyte. Then the coated part of the carbon fiber was immersed in the ionophore cocktail and the top of the micropipette was sealed with Loctite adhesive. More details on the fabrication of Mg^{2+} ISME, with solid contact, used in this work, are described elsewhere [49]. The Mg^{2+} ISME was calibrated using a 5 mmol L^{-1} NaCl solution as the base electrolyte, with standard solutions of $MgCl_2$ with a concentration range of 0.1 to 10^{-5} mol L^{-1}. A linear relationship between pMg and potential response was obtained, with a slope of −38 mV per pMg unit.

SECM potentiometric measurements were performed using the Mg^{2+} ISME and an Ag/AgCl/KCl (sat.) reference electrode as the electrochemical cell. Scans were performed in an *XY* plane parallel to the corroding surfaces. The ISME was placed at a height of approximately 50 μm above the studied surfaces, which was adjusted by means of a TV camcorder system.

2.4. Scanning vibrating electrode technique (SVET)

SVET maps were obtained using an Applicable Electronics instrument (New Haven, CT, USA), using a vibrating probe of Pt-—Ir with a spherical deposit of Pt black about 20 μm in diameter at its apex. The vibration frequencies of the probe were 190 Hz on the *X* axis, and 70 Hz on the *Z* axis, both with an amplitude of 20 μm. Scans were performed on the AA2098-T351 surfaces (embedded in epoxy resin) at a height of approximately 150 μm, established using the integrated video imaging system supplied with the equipment. SVET measurements were performed in a 5 mmol L^{-1} NaCl solution at ambient temperature. The investigated surfaces were left unbiased (effectively at their open circuit potential).

2.5. Localized electrochemical impedance spectroscopy (LEIS)

LEIS measurements were performed using a VersaSCAN equipment (AMETEK, Devon-Berwyn, PA, USA). The samples were embedded in epoxy resin. LEIS was used to measure the admittance (*A*) of AA2098-T351 surfaces when immersed in a 5 mmol L^{-1} NaCl solution. Admittance values were obtained by scanning the probe in the *X* and *Y* directions. The scanned area was 3.0 mm × 3.0 mm. The LEIS probe consisted of a dual microprobe: Pt-ring and Pt-micro-disk with a diameter of approximately 100 μm. An Ag/AgCl/KCl (sat.) was used as the reference electrode. The probe was placed at a height of approximately 100 μm above the surface, which was adjusted and monitored using a TV video camera system. A fixed frequency of 10 Hz and an amplitude of 10 mV were used to acquire the LEIS maps.

3. Results and discussion

3.1. Surface characterization

During the manufacture of Al-alloys, specifically in the rolling step, a deformed layer with different characteristics from the bulk material is formed, as shown in Fig. 1a. According to Fig. 1b, this layer is not homogenous; fine grains and particles which may have thicknesses of a few micrometers are observed. This inhomogeneous layer is known as the near-surface deformed layer (NSDL) [3–7]. NSDLs form due to the high levels of plastic strain induced in the surface plates of aluminum alloys during the rolling process [50].

In addition to microstructural changes, the rolling process can also induce defects and variations in the chemical composition of NSDL. Fig. 2 shows the top view features of the NSDL. Confocal laser scanning microscopy (CLSM) is useful for assessing surface morphology using a laser beam that scans the surface [51,52]. According to Fig. 2a, the surface of the as-received AA2098-T351 is heterogeneous and shows different bands in the rolling direction (indicated by red and yellow

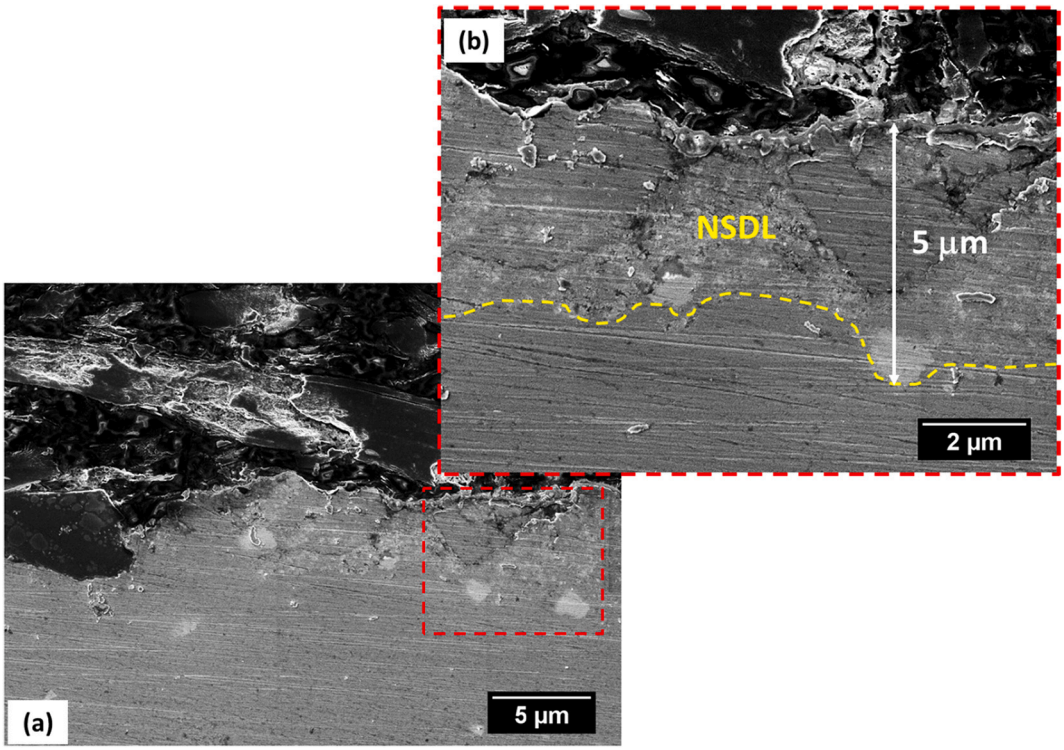

Fig. 1. (a) SEM cross section images of the near surface deformed layer (NSDL); (b) magnification image of the region marked with a square in (a).

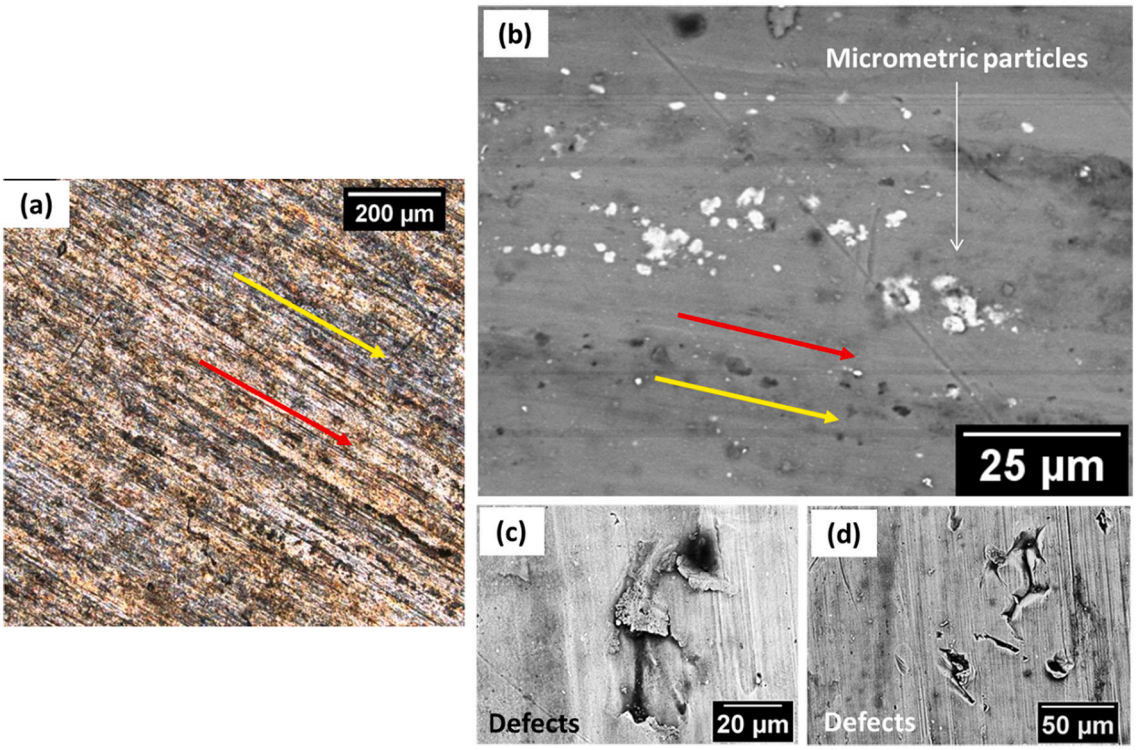

Fig. 2. (a) CLSM images of the AA2098-T351 as-received surface; (b-d) SEM magnification images showing top view features present in the NSDL.

arrows). The SEM images presented in Fig. 2b show that the different colors of the CLSM images are related to the oxide bands (yellow arrows) and the matrix (red arrows). In addition, micrometric particles can be observed on the surface of the as-received material. The contact of the rolls with the material also induces defects on the surface of the plate as shown in Fig. 2c-d. To characterize the particles and oxide bands on the as-received surface, EDX analysis was performed on the area shown in Fig. 2b. Fig. 3 shows that the oxide bands are rich in Mg. Moreover, segregations of Si and Zr are also observed. The micrometric particles of the alloy are enriched in Cu and Fe.

Fig. 4 shows the surface resulting from the removal of NSDL by polishing, noting that the underlying bulk alloy has a more homogeneous appearance (see Fig. 4a). Cu-—Fe enriched micrometric particles along the surface are observed in Fig. 4b. Besides the variation in composition of the micrometric particles with respect to the matrix, no segregation of other elements was observed on the polished surface, contrary to what was observed on the surface of the as-received material.

X-ray photoelectron spectroscopy (XPS) was performed to chemically characterize AA2098-T351 surfaces. High-resolution XPS spectra

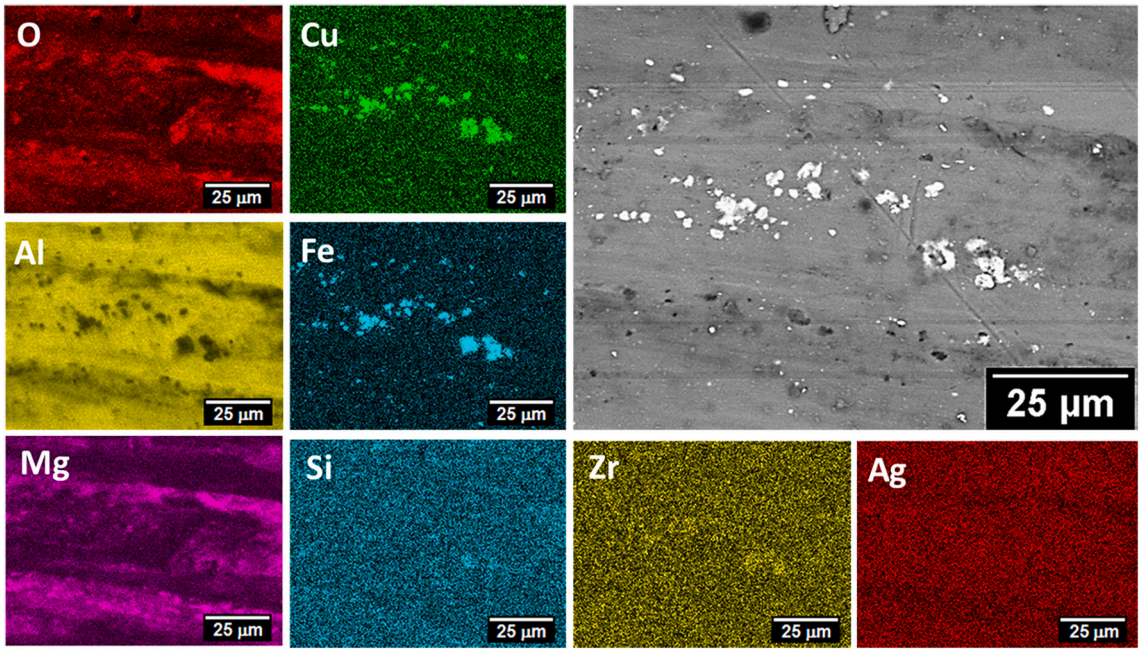

Fig. 3. EDX maps region shown in Fig. 2(b) giving the chemical composition of the as-received AA2098-T351 surface.

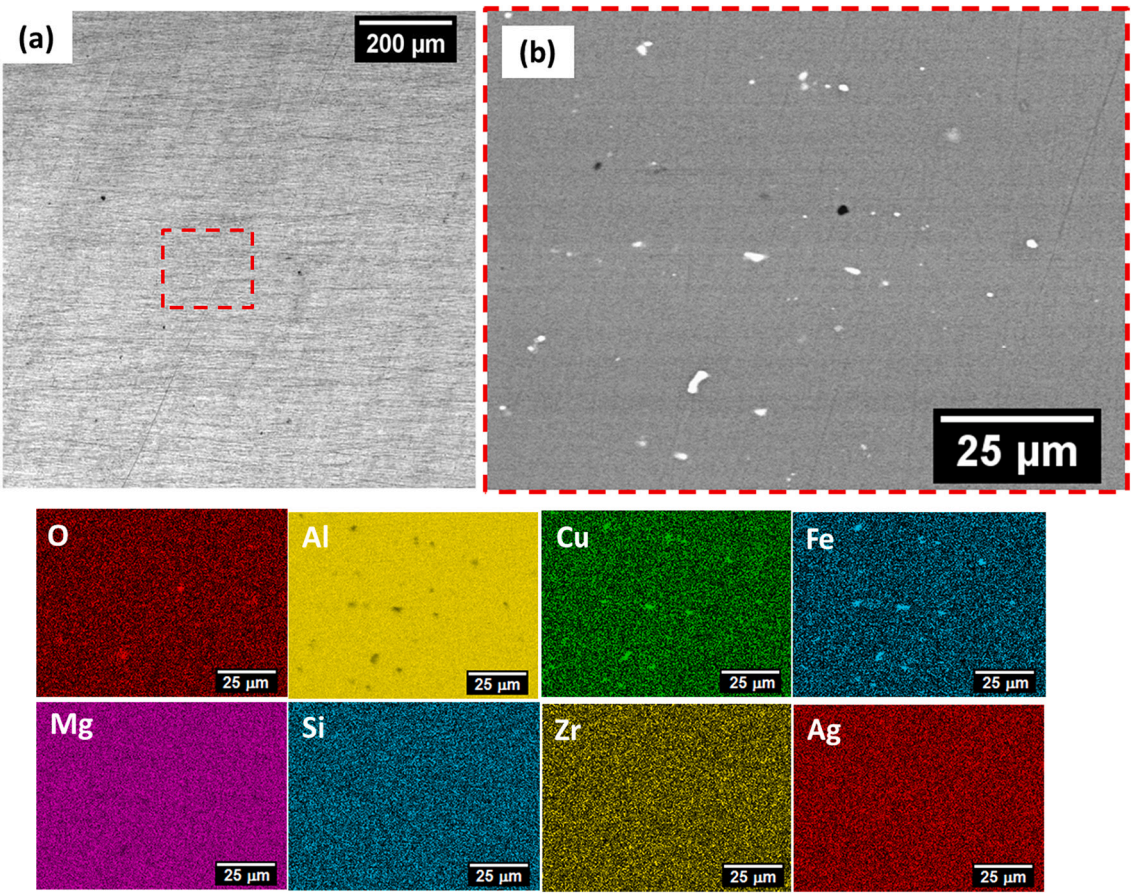

Fig. 4. (a) CLSM images of the polished AA2098-T351 surface; (b) high magnification SEM image of the region marked with a square in (a), and corresponding EDX maps showing the surface chemical composition of the polished surface.

of selected elements are shown in Fig. 5 for the as-received and polished conditions. According to Fig. 5a, the Al2p peak for the polished condition was higher than for the as-received state. As is known, two layers naturally form on the surface of Al-alloys: (i) an amorphous layer of Al_2O_3 and (ii) aluminum hydroxide. The thickness depends on the temperature and the chemical composition of the alloy [53]. Two Al2p peaks were observed for the polished condition, one related to the naturally formed oxide layer of Al_2O_3 at 74.1 eV and $Al(OH)_3$ at 75.2 eV, and the other related to metallic Al^0 at 71.8 eV [54,55]. This happens due to the activity of the freshly polished surface. Thus, if the alloy is exposed to the environment, the natural formation of Al oxide is favored. The absence of the metallic Al^0 peak for the as-received condition is due to the thickness of the surface layer, while the identification of metallic Al^0 in the polished surface indicates the presence of defects in the naturally formed oxide layer. The intensity of Cu2p, Fig. 5b, was higher for the as-received surface. The binding energies around 933.6 eV and 953.2 eV are related to the matrix and the micrometric particles [56]. According to EDX maps, the Cu signal is only related to micrometric particles (see Figs. 3 and 4), so the defects are responsible for the detection of Cu in solid solution [54] for both conditions. In addition, a significant reduction in the Mg content is observed on the polished surface (cf. Fig. 5c), which is due to the removal of NSDL. The EDX maps in Fig. 3 indicate that the as-received surface is enriched in magnesium oxide. However, the deconvolution of Mg1s signal in Fig. 5d for this material indicates the presence of peaks related to magnesium oxide (at 1304.2 eV) and metallic Mg^0 at the surface of the as-received alloy [57,58]. Mg enrichment in NSDL occurs due to outward migration of Mg atoms during hot working [4,59]. This occurs due to the high temperatures reached during the forming process, favoring the diffusion of Mg to the surface and its oxidation. This oxidation can occur directly by formation of MgO or by reduction of amorphous alumina, thus generating an oxide layer on the surface [50]. Additionally, metallic Mg^0 may be present which is highly reactive. Therefore, the differences in the chemical composition of the NSDL and the polished surface cause the two surfaces to exhibit different corrosion behavior. Moreover, mechanical grinding and polishing can also modify the properties of the surface and therefore affect its corrosion behavior [10,15,16].

3.2. Corrosion characterization

Corrosion courses on AA2098-T351 surfaces after different periods of immersion in 5 mmol L^{-1} NaCl solution are shown in Fig. 6. Corrosion products increasingly developed at specific sites on the as-received surface (cf. Fig. 6a-d), which were linked to Mg-enriched bands (yellow arrows). In addition, localized attack was related to the constituent particles, and severe localized corrosion (SLC; see areas circled in red) developed on the polished surface in Fig. 6e-h. The SLC sites of Fig. 7a-b were associated with hexagonal nanometric precipitates of the T1 phase [23,32]. This type of corrosion has certain characteristics, such as a cathodically protected region surrounding a corrosion ring and the evolution of hydrogen bubbles generated inside the pit [23,32,33]. Moreover, the attack exhibits preferential propagation, as shown by the yellow arrows in Fig. 7(b). This preferential attack is associated with the thermomechanical process, related to the stretching process which promotes dislocation bands which act as preferential sites for the precipitation of the T1 phase. In addition, the attack related to the constituent particles (trenching) of Fig. 7c, is observed from the first periods of immersion. On the polished surface, the accumulation of corrosion products occurs gradually near the SLC sites and in the regions associated with the micrometric particles.

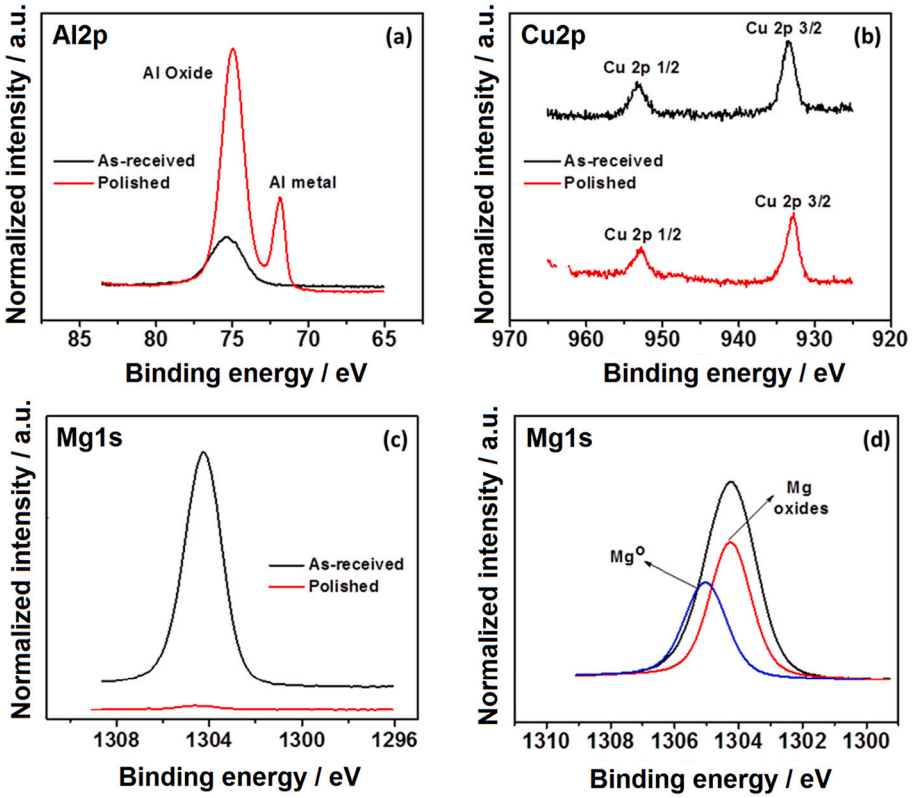

Fig. 5. High resolution XPS spectra of AA2098-T351 alloy in the as-received and polished conditions: (a) Al2p spectra; (b) Cu2p spectra; (c) Mg1s spectra; (d) deconvolution of the Mg1 spectra in (c).

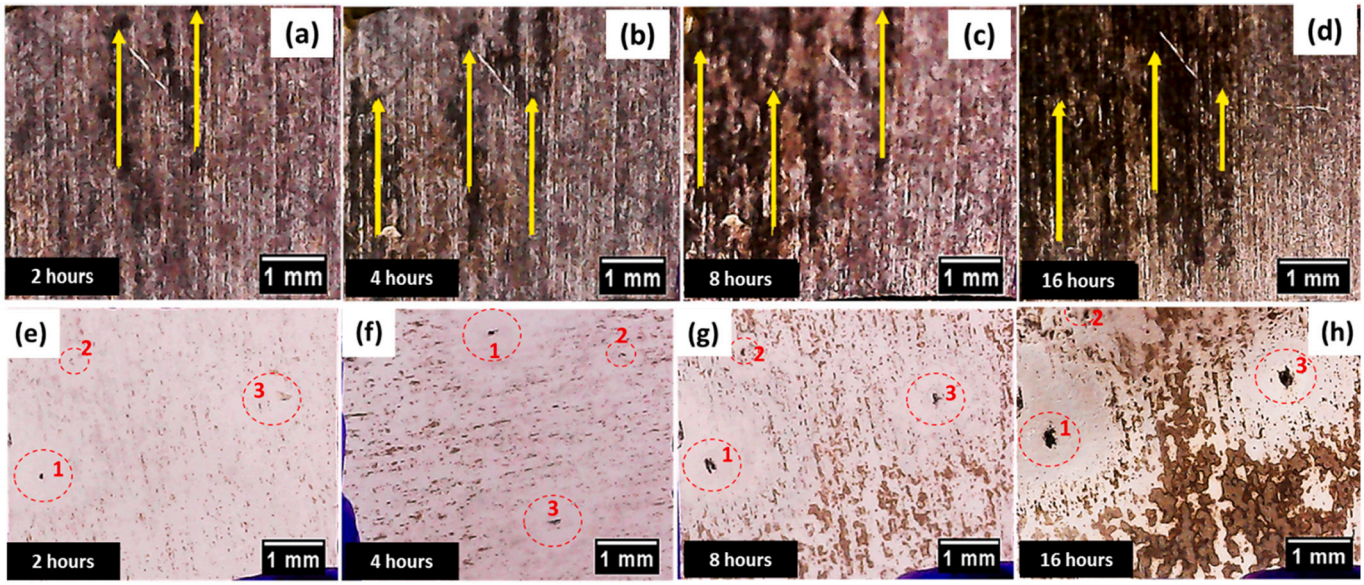

Fig. 6. Monitoring of the (a-d) as-received and (e-h) polished surfaces of the AA2098-T351 during immersion in 5 mmol L^{-1} NaCl solution for different periods of time as indicated.

For the as-received surface, Fig. 8a, the preferential direction of corrosion propagation is evidenced by the accumulation of corrosion products in the Mg-enriched bands (indicated by the red arrows). Observation of the surface after the corrosion test showed that penetration of the attack at these sites was shallow, but distributed over larger areas compared to the process on the polished surface (cf. Fig. 6). Trenching related to micrometric particles was also observed for the as-received sample in Fig. 8b. EDX analysis after the corrosion tests showed that bands of Mg oxide were still present on the surface according to Fig. 8c. XPS analysis of the polished AA2098-T351 surface after corrosion testing, Fig. 9, suggests that the detected Mg signal is related to the element in the matrix, once in this surface state, the NSDL has been removed. As observed in the high resolution XPS spectra of the alloy in the polished condition shown in Fig. 9c, the onset of corrosion increased the Cu content and decreased the Mg content at the surface. The increase in Cu2p peak signal is either related to Cu redeposition or Cu enrichment

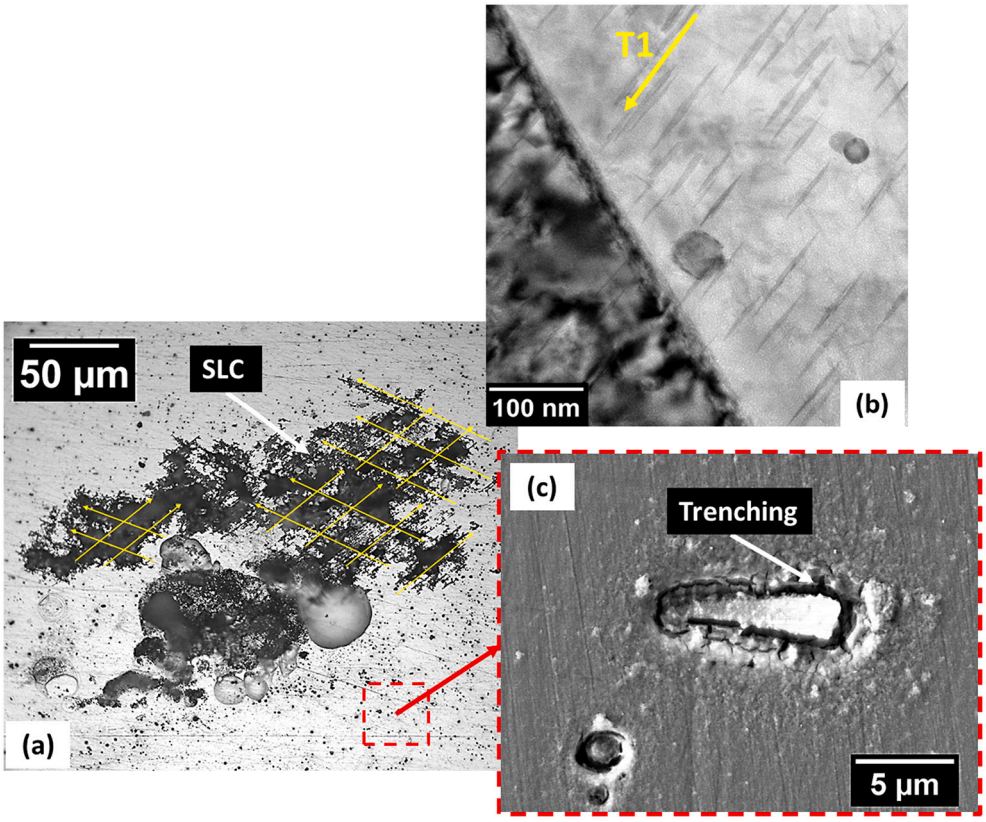

Fig. 7. Corrosion features observed on the polished surface of AA2098-T351 during immersion in 5 mmol L^{-1} NaCl solution. (a) Site of severe localized corrosion (SLC); (b) TEM bright image of the T1 phase in the [112] zone axis along ⟨220⟩ direction; (c) trenching attack related to micrometric particles.

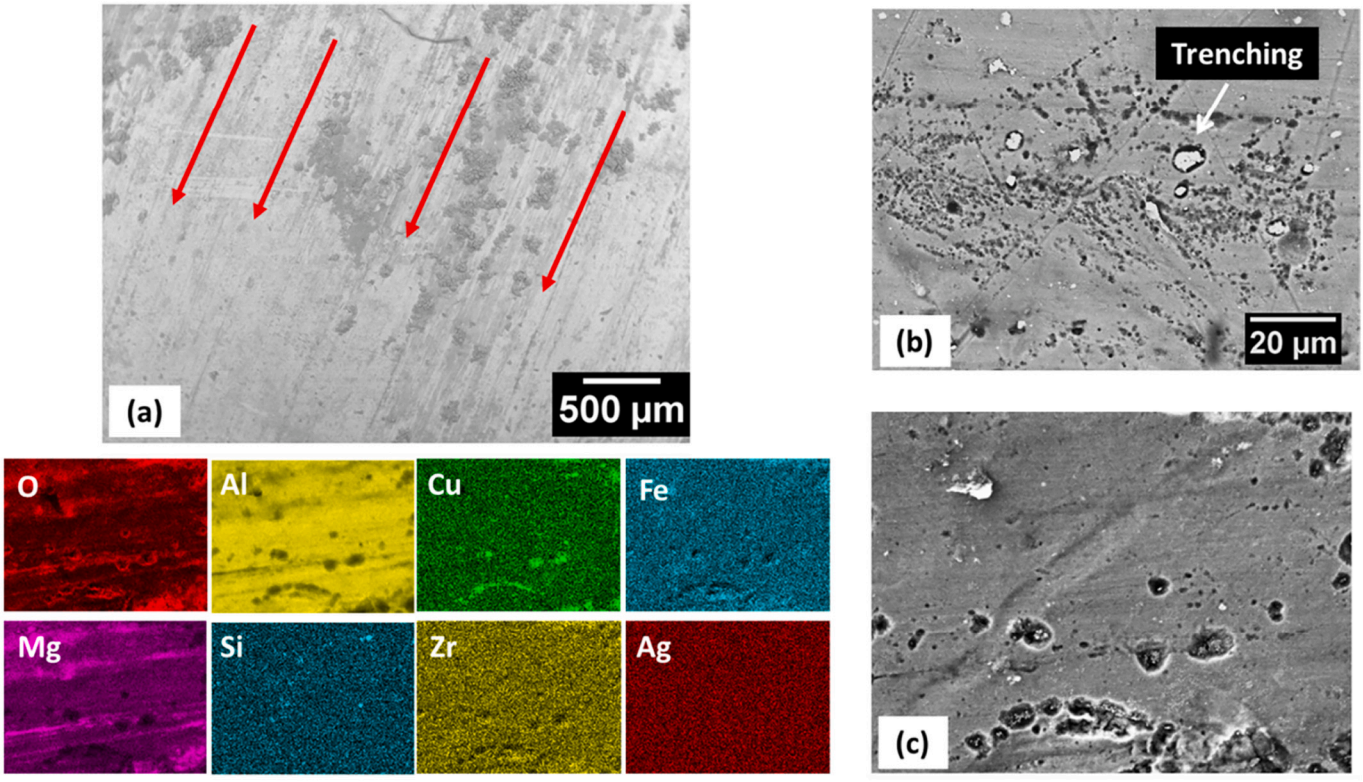

Fig. 8. Corrosion features observed in the as-received surface of the AA2098-T351 during immersion in 5 mmol L^{-1} NaCl solution. (a) Corrosion products formation in preferential sites; (b) superficial attack and trenching related to micrometric particles; (c) region monitored in the EDX analysis.

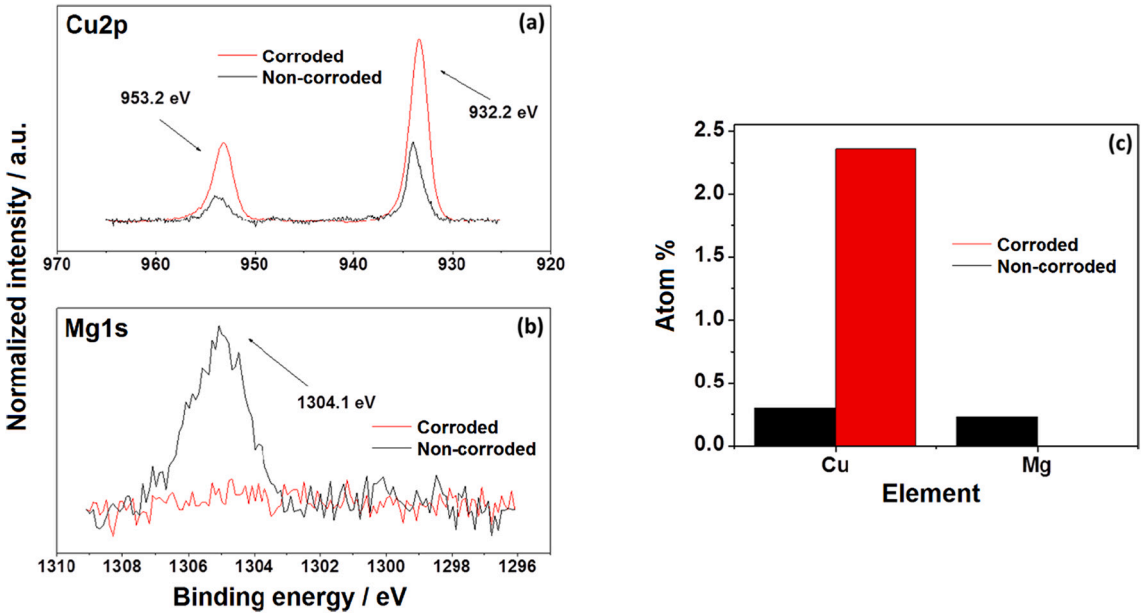

Fig. 9. Deconvolution of (a) Cu2p and (b) Mg1s signals for the polished AA2098-T351 before and after corrosion in 5 mmol L^{-1} NaCl solution; (c) Atomic percentage of the elements over the polished surface, before and after corrosion.

due to preferential dissolution of the less noble elements, which occurs at the cathodic and the anodic sites, respectively. On the other hand, the decrease in the Mg1s peak is linked to metal dissolution in the corrosive solution.

The depth profiles of the corroded areas in the two types of surface finishing are shown in Figs. 10 and 11 using profilometric images obtained after immersion in 5 mmol L^{-1} NaCl solution. The two distinct corrosion mechanisms related to the polished surface were readily observed. According to Fig. 10, the depth of attack on the polished surface related to SLC is greater than that associated with trenching. This suggests that the main corrosion mechanism on the polished surface is related to SLC. Profilometry images of the as-received AA2098-T351 surface are shown in Fig. 11. For this surface condition, the corroded surface exhibited regions with a depth of attack in the same order of the defective regions observed on the as-received surface before the corrosion test, and also in the same order as the previously reported trench-related attacks. The penetration profile confirmed the occurrence of a surface attack.

3.3. Electrochemical characterization

Spatial distributions of Mg^{2+} ions over as-received and polished

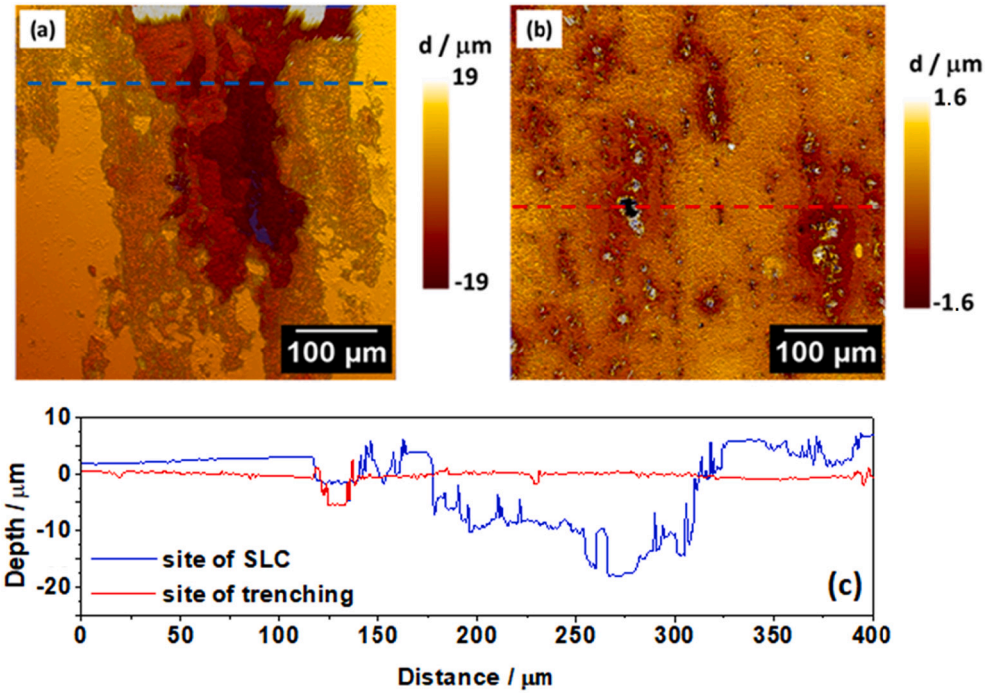

Fig. 10. Profilometry images of the polished AA2098-T351 surface after 24 h of immersion in 5 mmol L^{-1} NaCl solution: (a) severe localized corrosion site (SLC); (b) site of trenching associated with micrometric particles; (c) penetration profiles along the lines drawn in (a) and (b).

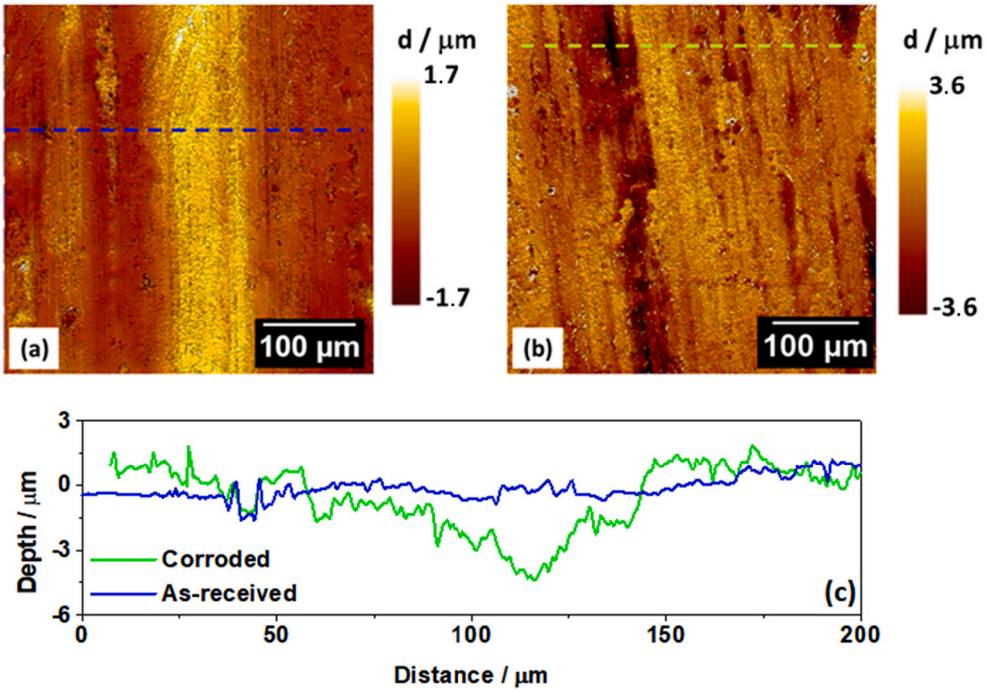

Fig. 11. Profilometry images of the as-received AA2098-T351 surface (a) before and (b) after 24 h of immersion in 5 mmol L^{-1} of NaCl solution; (c) penetration profiles along the lines drawn in (a) and (b).

AA2098-T351 surfaces after approximately 60 min exposure to 5 mmol L^{-1} NaCl solution were obtained using a Mg^{2+} ISME, shown in Fig. 12. The 2D array scan images show evidences of localized corrosion attacks on both surfaces. The lower and upper color scales for the 2D maps are an indication of the different Mg^{2+} activities for the different surfaces of the AA2098-T351 alloy under polished and as-received conditions. In Fig. 12, the red scale color indicates the regions with the most active domains for Mg^{2+} dissolution that occur at localized corrosion sites. The results corresponding to 60 min of immersion show a higher Mg^{2+} activity for the as-received surface compared to the polished one (cf. Fig. 12). Although the polished alloy has a lower Mg content in its surface composition, sites with measureable but lower Mg^{2+} activities are observed in Fig. 12a, confirming that Mg dissolution can also occur during corrosion of the material in this state. As shown in the high resolution XPS spectra of the polished alloy given in Fig. 9c, the Mg signal was detected and related to the element in the matrix. However, the corrosion process decreased the surface Mg content, so the decrease in the height of the Mg1s peak is related to its dissolution in the corrosive solution.

On the other hand, the higher Mg^{2+} activity observed in the as-received material is related to the Mg-enriched band present on the NSDL surface. This is associated with the chemical composition of NSDL, enriched in Mg and magnesium oxide (as seen in Figs. 3 and 5d). As shown in Fig. 6, corrosion of the as-received surface spread over the Mg-enriched bands. Mg is very active and is evenly distributed in oxide bands on the exposed as-received surface. Therefore, distributions with higher Mg^{2+} activities are observed for the as-received surface which exhibits more active surface corrosion associated with NSDL (see Fig. 11).

Fig. 13 shows maps acquired by the scanning vibrating electrode

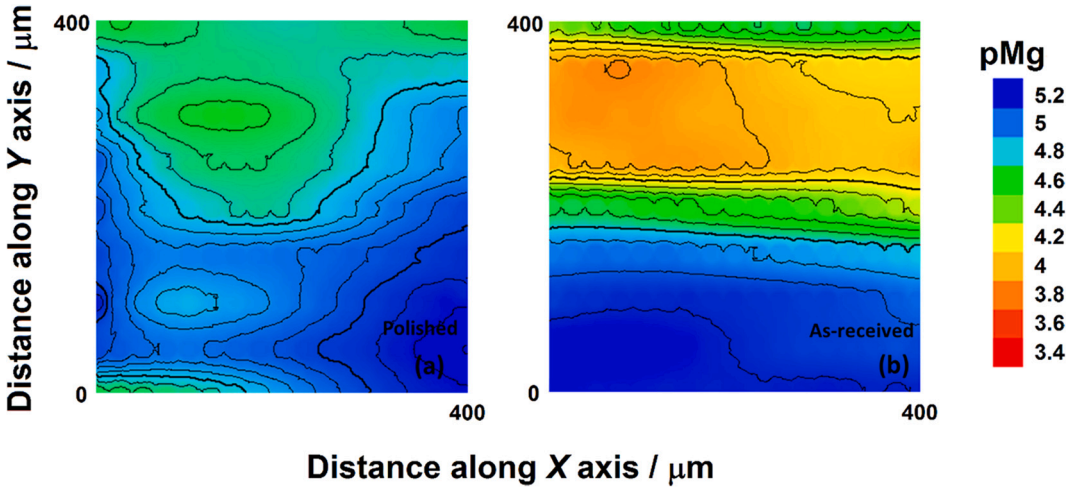

Fig. 12. SECM maps obtained above freely corroding AA2098-T351 surfaces in (a) polished and (b) as-received conditions. They were recorded after approximately 60 min of immersion in 5 mmol L^{-1} NaCl solution. The images were obtained using a Mg^{2+} ISME for potentiometric SECM operation. Tip-substrate distance: 50 µm; scan rate: 50 µm s^{-1}. ($pMg = -\log_{10} |Mg^{2+}|$).

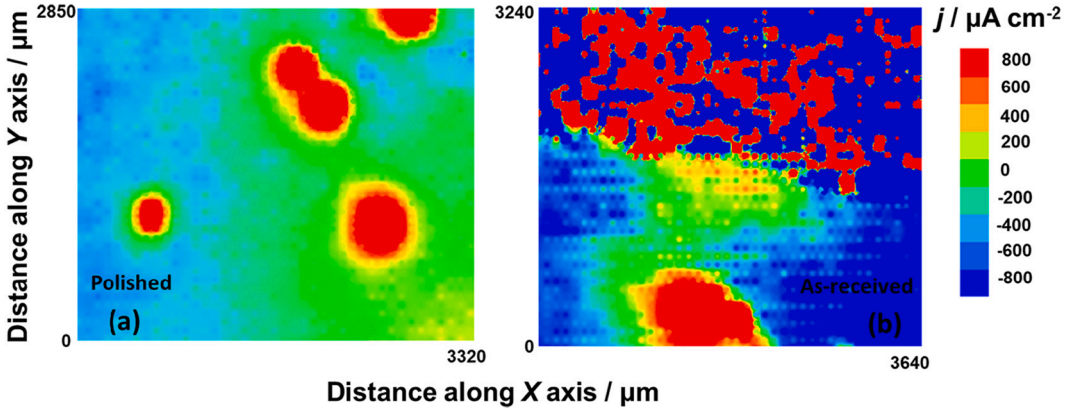

Fig. 13. SVET maps obtained above freely corroding AA2098-T351 surfaces in (a) polished and (b) as-received conditions. They were recorded after approximately 120 min of immersion in 5 mmol L^{-1} NaCl solution.

technique (SVET) of polished and as-received AA2098-T351 samples after immersion in 5 mmol L^{-1} NaCl solution for 2 h. For both surface conditions, corrosion activity was visible. In Fig. 13a, the development of SLC sites on the polished surface was observed. This finding confirms that the polished surface was more susceptible to the development of SLC sites than the as-received surface, consistent with the results shown in Fig. 6. Therefore, the highest anodic ionic currents were observed at the SLC sites and, as above noted, are associated with preferential attack of the T1 phase.

On the other hand, regions of high activity (i.e., red color) were also observed on the as-received surface in Fig. 13b. These have been associated with the Mg-enriched bands found for this surface finish. As shown above, Mg is very active and is evenly distributed over the exposed surface along the oxide bands (cf. Fig. 3). Therefore, measurement of anodic ion currents is also expected for the as-received condition, which mainly occurs in the Mg- and Mg-oxide-enriched NSDL. However, it is important to underline that the depth of the corrosion attack was less for this surface finish according to Fig. 11, which confirms a superficial attack. In addition, the as-received surface also exhibited regions with high cathodic activity (i.e. blue region), indicating that on average the corrosion activity was more intense on the polished surface.

LEIS maps recorded for polished and as-received surfaces in 5 mmol L^{-1} NaCl solution are shown in Fig. 14. Areas of higher admittances are related to regions of localized attack for both conditions. For the as-received surface finish shown in Fig. 14a, the regions of highest admittance correspond to band shapes with peaks of high admittance. However, the admittances for the as-received surface are smaller than for the polished surface given in Fig. 14b, i.e., about four times smaller than for the polished state. Moreover, the region of highest admittance values associated with the red color palette is related to an SLC site developed on the polished surface, in agreement with the SVET results shown in Fig. 13a. The observations described here, which were obtained using different localized microelectrochemical techniques show that SLC-related regions exhibited higher corrosion currents and higher electrochemical activities. On the other hand, since the corrosion mechanism of the as-received surface does not involve the development of SLC sites while the attack tends to be less penetrating (cf. Figs. 6a-d and 11), this surface gives lower admittances.

In summary, these results show that scanning microelectrochemical techniques are very useful for the electrochemical characterization of the alloy investigated in this study, and make it possible to differentiate the electrochemical behavior associated with the two types of surface conditions studied. According to the results, the corrosive attack on the polished alloy is more intense compared to the as-received alloy, showing a more electrochemically active surface corresponding to the absence of NSDL which exposes the bulk alloy to the corrosive environment.

4. Conclusions

The corrosion behavior and electrochemical activity of AA2098-T351 were investigated and surfaces conditions either presenting an NSDL region (i.e., as-received condition) or without it (e.g., polished surface finish) were compared.

Exposure tests and profilometry images showed that SLC sites did not develop on the as-received surfaces, unlike the polished surfaces. On the as-received surfaces, the outer layer of NSDL was enriched in Mg, as

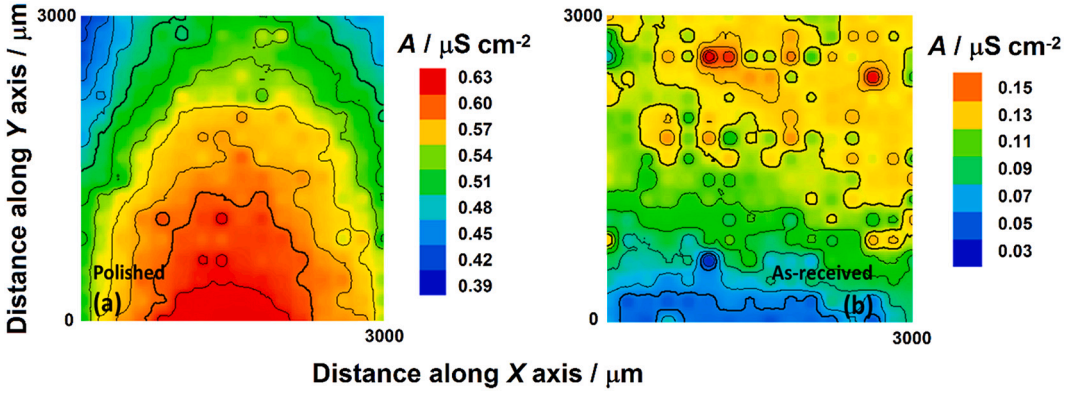

Fig. 14. LEIS maps obtained above AA2098-T351 surfaces in the (a) as-received and (b) polished conditions. They were recorded after approximately 120 min of immersion in 5 mmol L^{-1} NaCl solution.

confirmed by XPS and EDX analyzes. Higher distributions of Mg^{2+} ions in the adjacent electrolyte were monitored over the as-received AA2098-T351 surface by SECM in potentiometric operation using a Mg^{2+} ISME. SVET and LEIS results showed increased electrochemical activity associated to the SLC sites on the polished surface compared to the corrosion attack related to the as-received surface.

The results of this study demonstrated that the choice of localized scanning microelectrochemical techniques used in this work is very suitable for monitoring, with high spatial and chemical resolution, the electrochemical activities of the Al-Cu-Li alloys used in this study. In this way, different electrochemical behaviors were resolved for AA2098-T351 alloy samples with different surface finishes.

Data availability

The raw/processed data required to reproduce these findings cannot be shared at this time as the data also forms part of an ongoing study.

Declaration of Competing Interest

None.

Acknowledgements

The authors acknowledge Fundação de Amparo à Pesquisa do Estado de São Paulo- FAPESP (Proc. 2013/13235-6, Proc.2018/06880-6 and Proc. 2019/11427-1) for financial support, and funding from University of La Laguna and the Spanish Ministry of Science, Innovation and Universities (Madrid, Spain) under contract No. 2022/0000586. Authors are also grateful to CNEPEM/LNANO (Dr. Naga Vishnu Mogili) for support with TEM analysis.

References

[1] T. Dursun, C. Soutis, Recent developments in advanced aircraft aluminium alloys, Mater. Des. 56 (2014) 862–871, https://doi.org/10.1016/j.matdes.2013.12.002.
[2] R.J. Rioja, J. Liu, The evolution of Al-Li base products for aerospace and space applications, Metall. Mater. Transact. A: Phys. Metall. Mater. Sci. 43 (2012) 3325–3337, https://doi.org/10.1007/s11661-012-1155-z.
[3] G.M. Scamans, M.F. Frolish, W.M. Rainforth, Z. Zhou, Y. Liu, X. Zhou, G. E. Thompson, The ubiquitous beilby layer on aluminium surfaces, Surf. Interface Anal. 42 (2010) 175–179, https://doi.org/10.1002/sia.3204.
[4] X. Zhou, Y. Liu, G.E. Thompson, G.M. Scamans, P. Skeldon, J.A. Hunter, Near-surface deformed layers on rolled aluminum alloys, Metall. Mater. Transact. A: Phys. Metall. Mater. Sci. 42 (2011) 1373–1385, https://doi.org/10.1007/s11661-010-0538-2.
[5] Y. Liu, T. Hashimoto, X. Zhou, G.E. Thompson, G.M. Scamans, W.M. Rainforth, J. A. Hunter, Influence of near-surface deformed layers on filiform corrosion of AA3104 aluminium alloy, Surf. Interface Anal. 45 (2013) 1553–1557, https://doi.org/10.1002/sia.5232.
[6] J. Wang, X. Zhou, G.E. Thompson, J.A. Hunter, Y. Yuan, Microstructure evolution in the near-surface region during homogenization of a twin-roll cast AlFeMnSi alloy, Metall. Mater. Transact. A: Phys. Metall. Mater. Sci. 47 (2016) 4268–4275, https://doi.org/10.1007/s11661-016-3568-6.
[7] B. Liu, X. Zhang, X. Zhou, T. Hashimoto, J. Wang, The corrosion behaviour of machined AA7150-T651 aluminium alloy, Corros. Sci. 126 (2017) 265–271, https://doi.org/10.1016/j.corsci.2017.07.008.
[8] Z. Zhao, G.S. Frankel, The effect of temper on the first breakdown in AA7075, Corros. Sci. 49 (2007) 3089–3111, https://doi.org/10.1016/j.corsci.2007.02.004.
[9] Q.Z. Li, Y. Zuo, J.M. Zhao, Y.M. Tang, X.H. Zhao, J.P. Xiong, Corrosion behaviors of Ce- and Nd-modified anodic films on aluminum, Anti-Corrosion Methods Mater. 57 (2010) 238–243, https://doi.org/10.1108/00035591011075878.
[10] P.J.E. Forsyth, Sequence of corrosion attack of machining induced flow zone produced on some AI alloys that leads to rapid intergranular penetration, Mater. Sci. Technol. 14 (1998) 151–160, https://doi.org/10.1179/mst.1998.14.2.151.
[11] R. Ambat, A.J. Davenport, A. Afseth, G. Scamans, Electrochemical behavior of the active surface layer on rolled aluminum alloy sheet, J. Electrochem. Soc. 151 (2004) B53–B58, https://doi.org/10.1149/1.1635828.
[12] Y. Liu, X. Zhou, G.E. Thompson, T. Hashimoto, G.M. Scamans, A. Afseth, Precipitation and corrosion behaviour of nano-structured near-surface layers on an AA6111 aluminium alloy, J. Phys. Conf. Ser. 26 (2006) 103–106, https://doi.org/10.1088/1742-6596/26/1/024.
[13] Z. Zhao, G.S. Frankel, On the first breakdown in AA7075-T6, Corros. Sci. 49 (2007) 3064–3088, https://doi.org/10.1016/j.corsci.2007.02.001.
[14] Y. Liu, A. Laurino, T. Hashimoto, X. Zhou, P. Skeldon, G.E. Thompson, G. M. Scamans, C. Blanc, W.M. Rainforth, M.F. Frolish, Corrosion behaviour of mechanically polished AA7075-T6 aluminium alloy, Surf. Interface Anal. 42 (2010) 185–188, https://doi.org/10.1002/sia.3136.
[15] J. Seong, F. Yang, F. Scheltens, G.S. Frankel, N. Sridhar, Influence of the altered surface layer on the corrosion of AA5083, J. Electrochem. Soc. 162 (2015) C209–C218, https://doi.org/10.1149/2.0321506jes.
[16] S.-S. Wang, F. Yang, G.S. Frankel, Effect of altered surface layer on localized corrosion of aluminum alloy 2024, J. Electrochem. Soc. 164 (2017) C317–C323, https://doi.org/10.1149/2.1541706jes.
[17] T. Warner, Recently-developed aluminium solutions for aerospace applications, Mater. Sci. Forum 519–521 (2006) 1271–1278, https://doi.org/10.4028/www.scientific.net/MSF.519-521.1271.
[18] H.G. Salem, J.S. Lyons, Effect of equal channel angular extrusion on the microstructure and superplasticity of an Al-Li alloy, J. Mater. Eng. Perform. 11 (2002) 384–391, https://doi.org/10.1361/105994902770343908.
[19] P.S.S. De, R.S.S. Mishra, J.A.A. Baumann, Characterization of high cycle fatigue behavior of a new generation aluminum lithium alloy, Acta Mater. 59 (2011) 5946–5960, https://doi.org/10.1016/j.actamat.2011.06.003.
[20] M.X. Milagre, N.V. Mogili, U. Donatus, R.A.R. Giorjão, M. Terada, J.V.S. Araujo, C. S.C. Machado, I. Costa, On the microstructure characterization of the AA2098-T351 alloy welded by FSW, Mater. Charact. 140 (2018) 233–246, https://doi.org/10.1016/j.matchar.2018.04.015.
[21] J.V.S. Araujo, A.F.S. Bugarin, U. Donatus, C.S.C. Machado, F.M. Queiroz, M. Terada, A. Astarita, I. Costa, Thermomechanical treatment and corrosion resistance correlation in the AA2198 Al-Cu-Li alloy, Corros. Eng. Sci. Technol. 54 (2019) 575–586, https://doi.org/10.1080/1478422X.2019.1637077.
[22] W. Liu, A. Singh, Y. Lin, E.E. Ebenso, G. Tianhan, C. Ren, Corrosion inhibition of Al-alloy in 3.5% NaCl solution by a natural inhibitor: an electrochemical and surface study, Int. J. Electrochem. Sci. 9 (2014) 5560–5573.
[23] J.V.S. Araujo, U. Donatus, F.M. Queiroz, M. Terada, M.X. Milagre, M.C. de Alencar, I. Costa, On the severe localized corrosion susceptibility of the AA2198-T851 alloy, Corros. Sci. 133 (2018) 132–140, https://doi.org/10.1016/j.corsci.2018.01.028.
[24] U. Donatus, L.O. Berbel, I. Costa, Qualitative use of potentiodynamic polarization and anodic hydrogen evolution in the assessment of corrosion susceptibility in AA2198-T851 Al–Cu–Li alloy, Mater. Corros. 69 (2018) 1375–1388, https://doi.org/10.1002/maco.201810108.
[25] R.G. Buchheit Jr., J.P. Moran, G.E. Stoner, Localized corrosion behavior of aIloy 2090- the role of microstructural heterogeneity, Corrosion. 46 (1990) 610–617, https://doi.org/10.5006/1.3585156.
[26] V. Proton, J. Alexis, E. Andrieu, C. Blanc, J. Delfosse, L. Lacroix, G. Odemer, Influence of post-welding heat treatment on the corrosion gehavior of a 2050-T3 aluminum-copper-lithium alloy friction stir welding joint, J. Electrochem. Soc. 158 (2011) C139, https://doi.org/10.1149/1.3562206.
[27] V. Proton, J. Alexis, E. Andrieu, J. Delfosse, A. Deschamps, F. de Geuser, M. C. Lafont, C. Blanc, The influence of artificial ageing on the corrosion behaviour of a 2050 aluminium-copper-lithium alloy, Corros. Sci. 80 (2014) 494–502, https://doi.org/10.1016/j.corsci.2013.11.060.
[28] Y. Ma, X. Zhou, W. Huang, Y. Liao, X. Chen, X. Zhang, G.E. Thompson, Crystallographic defects induced localised corrosion in AA2099-T8 aluminium alloy, Corros. Eng. Sci. Technol. 50 (2015) 420–424, https://doi.org/10.1179/1743278214Y.0000000237.
[29] X. Zhang, X. Zhou, T. Hashimoto, B. Liu, C. Luo, Z. Sun, Z. Tang, F. Lu, Y. Ma, Corrosion behaviour of 2A97-T6 Al-Cu-Li alloy: the influence of non-uniform precipitation, Corros. Sci. 132 (2018) 1–8, https://doi.org/10.1016/j.corsci.2017.12.010.
[30] Y. Ma, X. Zhou, W. Huang, G.E. Thompson, X. Zhang, C. Luo, Z. Sun, Localized corrosion in AA2099-T83 aluminum-lithium alloy: the role of intermetallic particles, Mater. Chem. Phys. 161 (2015) 201–210, https://doi.org/10.1016/j.matchemphys.2015.05.037.
[31] Y. Ma, X. Zhou, Y. Liao, Y. Yi, H. Wu, Z. Wang, W. Huang, Localised corrosion in AA 2099-T83 aluminium-lithium alloy: the role of grain orientation, Corros. Sci. 107 (2016) 41–48, https://doi.org/10.1016/j.corsci.2016.02.018.
[32] U. Donatus, J.V.S. Araujo, C.S.C. Machado, N.V.V. Mogili, R.A. Antunes, I. Costa, The effect of manufacturing process induced near-surface deformed layer on the corrosion behaviour of AA2198-T851 Al–Cu–Li alloy, Corros. Eng. Sci. Technol. 54 (2018) 205–215, https://doi.org/10.1080/1478422X.2018.1558932.
[33] R.M.P. da Silva, M.X. Milagre, L.A. de Oliveira, U. Donatus, R.A. Antunes, I. Costa, The local electrochemical behavior of the AA2098-T351 and surface preparation effects investigated by scanning electrochemical microscopy, Surf. Interface Anal. 51 (2019) 982–992, https://doi.org/10.1002/sia.6682.
[34] M.X. Milagre, U. Donatus, C.S.C. Machado, J.V.S. Araujo, R.M.P. da Silva, B.V.G. de Viveiros, A. Astarita, I. Costa, Comparison of the corrosion resistance of an Al–Cu alloy and an Al–Cu–Li alloy, Corros. Eng. Sci. Technol. 54 (2019) 402–412, https://doi.org/10.1080/1478422X.2019.1605472.
[35] R.M.P. da Silva, J. Izquierdo, M.X. Milagre, A.M. Betancor-Abreu, L.A. de Oliveira, R.A. Antunes, R.M. Souto, I. Costa, On the local corrosion behavior of coupled welded zones of the 2098-T351 Al-Cu-Li alloy produced by friction stir welding (FSW): an amperometric and potentiometric microelectrochemical investigation, Electrochim. Acta 373 (2021), 137910, https://doi.org/10.1016/j.electacta.2021.137910.
[36] F. Zou, D. Thierry, Localized electrochemical impedance spectroscopy for studying the degradation of organic coatings, Electrochim. Acta 42 (1997) 3293–3301, https://doi.org/10.1016/S0013-4686(97)00180-1.
[37] V. Upadhyay, D. Battocchi, Localized electrochemical characterization of organic coatings: a brief review, Prog. Org. Coat. 99 (2016) 365–377, https://doi.org/10.1016/j.porgcoat.2016.06.012.

[38] A.S. Nguyen, N. Pébère, A local electrochemical impedance study of the self-healing properties of waterborne coatings on 2024 aluminium alloy, Electrochim. Acta 222 (2016) 1806–1817. doi:https://doi.org/10.1016/j.electacta.2016.11.152.
[39] J.B. Jorcin, C. Blanc, N. Pébère, B. Tribollet, V. Vivier, Galvanic coupling between pure copper and pure aluminum: experimental approach and mathematical model, J. Electrochem. Soc. 155 (2008) C46–C51, https://doi.org/10.1149/1.2803506.
[40] L. Lacroix, C. Blanc, N. Pébère, B. Tribollet, V. Vivier, Localized approach to galvanic coupling in an aluminum–magnesium system, J. Electrochem. Soc. 156 (2009) C259–C265, https://doi.org/10.1149/1.3148833.
[41] C.P. de Abreu, I. Costa, G. de Melo, P. Nadine, B. Tribollet, V. Vivier, Multiscale electrochemical study of welded Al alloys joined by friction stir welding, J. Electrochem. Soc. 164 (2017) C735–C746, https://doi.org/10.1149/2.0391713jes.
[42] G. Acosta, L. Veleva, D. de la Fuente, Mapping the initial corrosion activity of aluminium alloy 2024-T3 in diluted substitute ocean water by localized electrochemical impedance spectroscopy, Mater. Corros. 69 (2018) 1368–1374, https://doi.org/10.1002/maco.201810109.
[43] F.M. Queiroz, U. Donatus, O.M.P. Ramirez, J.V.S. Araujo, B.V.G. de Viveiros, S. Lamaka, M. Zheludkevich, M. Masoumi, V. Vivier, I. Costa, H.G. de Melo, Effect of unequal levels of deformation and fragmentation on the electrochemical response of friction stir welded AA2024-T3 alloy, Electrochim. Acta 313 (2019) 271–281, https://doi.org/10.1016/j.electacta.2019.04.137.
[44] R. Akid, M. Garma, Scanning vibrating reference electrode technique: a calibration study to evaluate the optimum operating parameters for maximum signal detection of point source activity, Electrochim. Acta 49 (2004) 2871–2879, https://doi.org/10.1016/j.electacta.2004.01.069.
[45] A.J. Bard, G. Denuault, C. Lee, D. Mandler, D.O. Wipf, Scanning electrochemical microscopy - a new technique for the characterization and modification of surfaces, Acc. Chem. Res. 23 (1990) 357–363, https://doi.org/10.1021/ar00179a002.
[46] R.M. Souto, J. Izquierdo, Progress in scanning electrochemical microscopy by coupling potentiometric and amperometric measurement modes, in: A. Méndez-Vilas (Ed.), Current Microscopy Contributions to Advances in Science and Technology Vol. 2, Formatex Research Center, Badajoz (Spain), 2012, pp. 1407–1415.
[47] J.V.S. Araujo, R.M.P. da Silva, U. Donatus, C.S.C. Machado, I. Costa, Microstructural, electrochemical and localized corrosion characterization of the AA2198-T851 alloy, Mater. Res. 23 (2020), e20200161, https://doi.org/10.1590/1980-5373-mr-2020-0161.
[48] R.M.P. da Silva, J. Izquierdo, M.X. Milagre, A.M. Betancor-Abreu, I. Costa, R. M. Souto, Use of amperometric and potentiometric probes in scanning electrochemical microscopy for the spatially-resolved monitoring of severe localized corrosion sites on aluminum alloy 2098-T351, Sensors 21 (2021) 1132, https://doi.org/10.3390/s21041132.
[49] J. Izquierdo, A. Kiss, J.J. Santana, L. Nagy, I. Bitter, H.S. Isaacs, G. Nagy, R. M. Souto, Development of Mg^{2+} ion-selective microelectrodes for potentiometric scanning electrochemical microscopy monitoring of galvanic corrosion processes, J. Electrochem. Soc. 160 (2013) C451–C459, https://doi.org/10.1149/2.001310jes.
[50] K. Li, X.R. Zhou, G.E. Thompson, J.A. Hunter, Y.D. Yuan, Evolution of near-surface deformed layers on AA3104 aluminium alloy, Mater. Sci. Forum 765 (2013) 358–362, https://doi.org/10.4028/www.scientific.net/MSF.765.358.
[51] M.A. Alodan, W.H. Smyrl, Detection of localized corrosion using fluorescence microscopy, J. Electrochem. Soc. 144 (1997) L282–L284, https://doi.org/10.1149/1.1838010.
[52] N. Llorca-Isern, M. Puig, M. Español, Improving the methodology for coating defects detection, J. Therm. Spray Technol. 8 (1999) 73–78, https://doi.org/10.1361/105996399770350593.
[53] J. Zähr, S. Oswald, M. Türpe, H.J. Ullrich, U. Füssel, Characterisation of oxide and hydroxide layers on technical aluminum materials using XPS, Vacuum 86 (2012) 1216–1219, https://doi.org/10.1016/j.vacuum.2011.04.004.
[54] A. Uhart, J.C. Dupin, J.P. Bonino, D. Gonbeau, J. Esteban, J.B. Ledeuil, F. Ansart, An auger and XPS survey of cerium active corrosion protection for AA2024-T3 aluminum alloy, Appl. Surf. Sci. 390 (2016) 751–759, https://doi.org/10.1016/j.apsusc.2016.08.170.
[55] L. Muñoz, F. Pineda, C. Martínez, M. Sancy, M. Urzua, M. Flores, M.V. Encinas, M. A. Páez, Improving the interaction between aluminum surfaces and polymer coatings, Surf. Coat. Technol. 358 (2019) 435–442, https://doi.org/10.1016/j.surfcoat.2018.11.051.
[56] S.A. Kulinich, A.S. Akhtar, P.C. Wong, K.C. Wong, K.A.R. Mitchell, Growth of permanganate conversion coating on 2024-Al alloy, Thin Solid Films 515 (2007) 8386–8392, https://doi.org/10.1016/j.tsf.2007.04.164.
[57] N.C. Haider, J. Alonso, W.E. Swartz, Valence and core electron spectra of Mg in MgO in evoporated thin films, Zeitschrift Naturfor. A - A J. Phys. Sci. 30 (1975) 1485–1490, https://doi.org/10.1515/zna-1975-1119.
[58] J.E. Qu, M. Ascencio, L.M. Jiang, S. Omanovic, L.X. Yang, Improvement in corrosion resistance of WE43 magnesium alloy by the electrophoretic formation of a ZnO surface coating, J. Coat. Technol. Res. 16 (2019) 1559–1570, https://doi.org/10.1007/s11998-019-00212-7.
[59] K. Shimizu, G.M. Brown, K. Kobayashi, P. Skeldon, G.E. Thompson, G.C. Wood, The early stages of high temperature oxidation of an Al-0.5 wt% Mg alloy, Corros. Sci. 40 (1998) 557–575, https://doi.org/10.1016/S0010-938X(97)00153-4.